Structure and charge transport of amorphous Cu-doped Ta₂O₅: An *ab initio* study

Rajendra Thapa [*]

Department of Physics and Astronomy, Nanoscale and Quantum Phenomena Institute (NQPI), Ohio University, Athens, Ohio 45701, USA

Bishal Bhattarai [†]

Department of Physics, Missouri University of Science and Technology, Rolla, Missouri 65409, USA

M. N. Kozicki [‡]

Department of Electrical, Computer and Energy Engineering, Arizona State University, Tempe, Arizona 85287, USA

Kashi N. Subedi[§] and D. A. Drabold [¶]

Department of Physics and Astronomy, Ohio University, Athens, Ohio 45701, USA

In this paper, we present *ab initio* computer models of Cu-doped amorphous Ta₂O₅, a promising candidate for conducting bridge random access memory memory devices, and study the structural, electronic, charge transport, and vibrational properties based on plane-wave density-functional methods. We offer an atomistic picture of the process of phase segregation/separation between Cu and Ta₂O₅ subnetworks. Electronic calculations show that the models are conducting with extended Kohn-Sham orbitals around the Fermi level. In addition to that, we also characterize the electronic transport using the Kubo-Greenwood formula modified suitably to calculate the space-projected conductivity (SPC) [K. Prasai, K. N. Subedi, K. Ferris, P. Biswas, and D. A. Drabold, Phys. Stat. Solidi Rapid Res. Lett. **12**, 1800238 (2018)]. Our SPC calculations show that Cu clusters and undercoordinated Ta adjoining the Cu are the conduction-active parts of the network. We also report information about the dependence of the electrical conductivity on the connectivity of the Cu submatrix. Vibrational calculations for one of the models has been undertaken with an emphasis on localization and animation of representative modes.

I. INTRODUCTION

Novel nonvolatile memory devices are an area of active inquiry. Research on ferroelectric random access memory and magnetoresistive random access memory have been limited due to underlying technological and scalability problems [1]. Meanwhile, study of nonvolatile memory, based on electrically switchable resistance or resistive random access memory (ReRAM), has gained considerable interest. The first studies of such resistive switching was reported in the 1960s and was based on oxides in a metal-ion-metal framework with formation/dissolution (SET/RESET) of filament electrochemical in nature [2]. Among ReRAM's, electrochemical metallization mechanism or conductive bridging random access memory (CBRAM) which utilizes the electrochemical dissolution of an active electrode material such as Cu or Ag for SET/RESET mechanism has shown particular promise. In CBRAM, transition metals in their ionic state are converted to a conducting filament by applying a suitable electric field, which, on reversal, destroys the filament resulting in a resistive state. Several possible candidates for solid electrolytes have been studied elsewhere [3–8]. Amorphous tantalum pentoxide/amorphous tantala (a-Ta₂O₅) has been investigated as a possible candidate for memory devices, antireflection coatings, and optical waveguides due to its high dielectric constant, high refractive index, chemical and thermal stability [9–11]. Cu-doped a-Ta₂O₅ shows promising properties for CBRAM-based memory devices.

Several experiments as well as calculations [12–15] have been carried out to understand conduction mechanisms in Ta₂O₅ materials. In these studies [12,14,15], Ag, Cu, and Pt metals were used as electrodes while in one Xiao *et al.* [13] used Cu nanowires of different diameters inserted into the low-density Ta₂O₅ host to study transport and electronic properties of Ta₂O₅ as an electrolyte. These papers indicate that metal filaments are responsible for conduction. It has been reported that conduction paths in different electrolytes differ qualitatively. Metals such as Cu form clusters, leading to a conducting filament in oxides, while no such clustering is observed in chalcogenide-based electrolytes [16]. Since a complete investigation of Cu-doped Ta₂O₅ has not yet been reported, we provide here a thorough investigation amid growing research to test its candidacy as a possible electrolyte for CBRAM technologies.

————————

[*]rt887917@ohio.edu

[†]bb6fq@mst.edu

[‡]michael.kozicki@asu.edu

[§]ks173214@ohio.edu

[¶]drabold@ohio.edu

In this paper, we investigate amorphous Cu-doped a-Ta_2O_5. We provide insights into structural properties, coordination statistics, electronic, vibrational properties and visualize conduction/current paths by computing the space-projected conductivity (SPC) [16]. We elucidate the atomistic mechanisms of phase segregation and track the emergence of Cu clusters as the melt cools. The rest of paper is organized as follows. In Sec. II, we discuss the computational methodology used to generate our models. This is followed by validation of the generated models with particular attention to the structural, electronic, vibrational, and thermal properties in Sec. III. In Sec. IV we present the conclusions of our work and future research directions.

II. METHODOLOGY AND MODELS

We prepare two 210-atom models of a-$(Ta_2O_5)_{0.80}Cu_{0.20}$ cooled at different rates by utilizing melt-quenching within the *ab initio* molecular dynamics (AIMD) method. The initial density for both of the models was chosen to be that of amorphous tantala ($\rho = 7.79$ gm/cc), consistent with experimental [17,18] and theoretical studies [13]. We have performed molecular dynamics simulations using *ab initio* plane-wave code Vienna *Ab initio* Software Package (VASP) [19–21] with projector-augmented wave method [22] and employed the *Perdew-Burke-Ernzerhof* [23] exchange-correlation functional. The Γ point is used to sample the Brillouin zone. A plane-wave cut-off of 500 eV, a time step of 3.0 fs, and Nosé thermostat [24–26] was used to control the temperature.

All *ab initio* computer simulations of amorphous materials make severe approximations for system size and quench rates. Ours is no exception. To gauge the effects of our fast quench rates, we made three models using different rates. All three have exhibit the same qualitative behavior and essentially similar microstructure. The one interesting departure involves the structure of Cu aggregates, as we discuss in detail, including animations in the Supplemental Material [27].

A. Model I

We fabricated a starting model of 48 Ta, 120 O, and 42 Cu atoms with random initial positions (with no atoms closer than 2 Å) in a cubic box of side 14.14 Å. This model was then taken through a *melt quench* (MQ) [28] cycle. First, the system was heated well above melting point to form a liquid at 6000 K. This liquid melt was then equilibrated at 6000 K for 18 ps, cooled to 3000 K in 9 ps, equilibrated at 3000 K for 6 ps, and then cooled to 300 K for 15 ps. This summed up to a total simulation time of 57 ps. The cell volume was relaxed to obtain zero pressure models. This zero-pressure relaxation produced a volume rise of 2.09% yielding an optimized density of 7.63 gm/cc.

B. Model II

Another MQ model, with slower cooling rate around the melting point of Ta_2O_5, was made. This model started with the melt of Model I cooled to 3000 K and was further cooled to 300 K in 24 ps without any intermediate equilibration. The total simulation time was 60 ps.
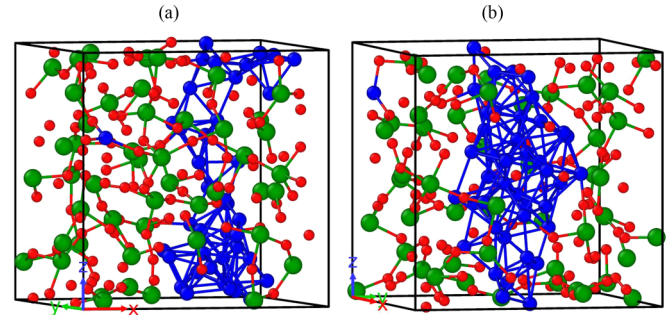

FIG. 1. The structure of Model I (a) and Model II (b) consists of tantalum atoms bonded to five, six, and seven oxygen atoms to form a mixture of edge-sharing, corner-sharing, and face-sharing polyhedra and a connected subnetwork of Cu atoms. The Cu network grows in the interstitial space between Ta-O polyhedra. Cu, Ta, and O atoms are shown in blue, green and red, respectively, and the same "color nomenclature" will be used throughout the paper.

After dynamical arrest, conjugate-gradient relaxation was applied until the magnitude of the force on each atom was reduced to less than 0.01 eV/Å. Zero-pressure relaxation increased the volume by 2.39% and the density was optimized to 7.61 gm/cc. A third model, cooled faster than the models discussed here, has been described in the supplemental material, to provide some insight into the influence of the quench rate on the network topology.

For simplicity and consistency, we follow the same "color nomenclature" for the atomic species: Ta, O, and Cu atoms are shown in green, red, and blue, respectively.

III. RESULTS AND DISCUSSION

A. Structural properties

The structure is elucidated in Figs. 1 and 2. As shown in Fig. 2, the radial distribution function (RDF) for both models has a first peak at 1.95 Å, which arises from the dominant Ta-O bonds and corresponds to the Ta-O bond length. This peak is in agreement with experiments [17,29] for pure a-Ta_2O_5 and previous DFT calculations [12] for Cu-doped tantala as well which suggests that the introduction of Cu to the network does not significantly change the local environment around the Ta atoms, i.e., the dominance of Ta-O octahedra in the structure persists even after Cu doping. This finding is also supported by low Cu-O coordinations. Introduction of Cu, however, steals some O coordination from Ta, as seen in Table I, and these undercoordinated Ta atoms have a significant role in conduction which will be explained later.

The Ta-Ta correlations also remain unaffected by Cu doping but a strong peak, at 2.48 Å, in the Cu-Cu correlations suggests the formation of Cu clusters in the system, as seen in Fig. 1, which can be attributed to the ionicity of the Ta-O bonds [30] that drives the Cu atoms to cluster.

Previously, clustering of Cu in ionic host (a-Al_2O_3) has been reported [16]. This strong Cu-Cu correlation suggests that Cu atoms preferentially bond with themselves, consistent with the coordination statistics. In contrast, zirconia-doped tanatala shows no Zr clustering and the metal atoms distribute themselves homogenously with no metal-metal pair closer
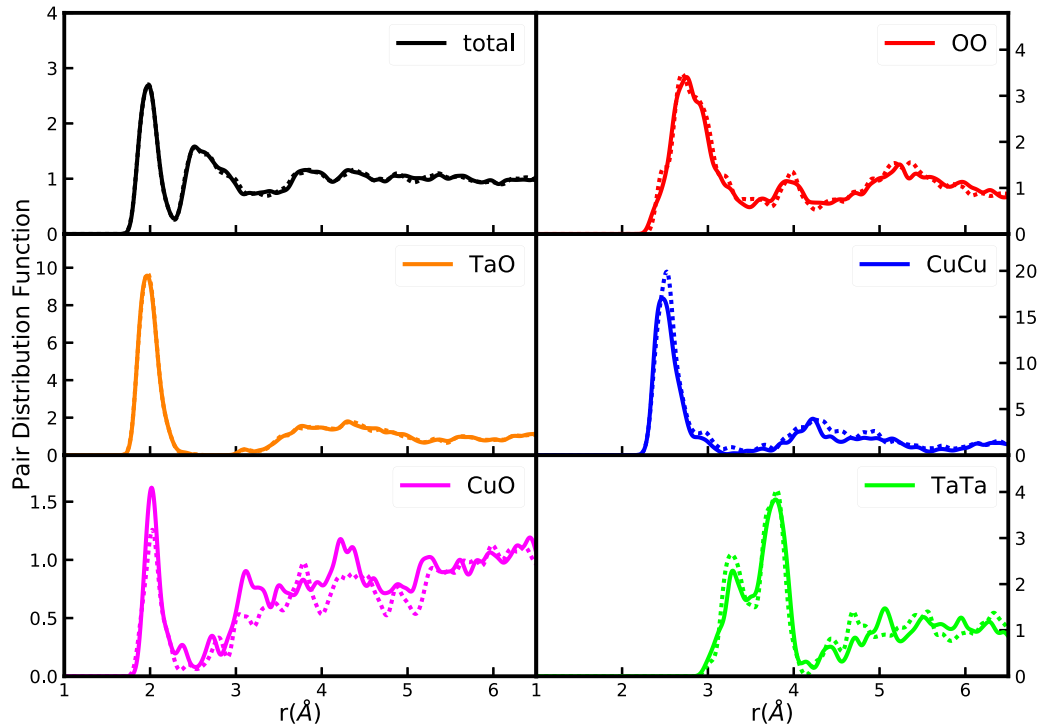
FIG. 2. Pair distribution function for Model I (solid line) and Model II (dotted line). The total pair distribution function [g(r)] is almost the same for both the models. There is, however, a slight change in the Cu-Cu and Cu-O partial correlations.

than 2.9 Å [11]. It is quite interesting that our calculations "naturally" produce connected Cu "wires" that are extended in space (considering the periodic boundary conditions), not by modeler's "installation" but as a direct and unbiased consequence of the melt-quench simulations themselves.

Two peaks are worth mentioning in the Ta-Ta correlation: The first at around 3.3 Å, and the second around 3.8 Å, first because they provide an idea of the how the Ta-O octahedra are connected and, second, because they are implicated in mechanical loss for Laser Interferometer Gravity Wave Observatory application [11]. The former comes from the joint contribution of face and edge-shared octahedral connection while the latter derives from the corner-shared connection of the octahedra.

The coordination statistics of the models in Table I largely serve to validate the findings of the RDF and the correlations

TABLE I. Average coordination number (n) and its distribution among different species. Coordination is counted only if the distance between the atoms is no more than the sum of their covalent radius within a tolerance of 0.1 Å. Covalent radii for Ta, O, and Cu are taken as 1.70 Å, 0.73 Å, and 1.32 Å, respectively.

	Atom	n	n(Ta)	n(O)	n(Cu)
	Ta	7.96	1.75	5.52	0.69
Model I	O	2.44	2.21	0.00	0.23
	Cu	7.17	0.79	0.67	5.71
	Ta	8.00	1.92	5.60	0.48
Model II	O	2.45	2.24	0.00	0.21
	Cu	7.48	0.55	0.60	6.33

between different species. It also suggests that, as we lower the cooling rate, the Cu-Cu coordination increases while the Cu-O coordination decreases within the admitted limitations of rapid quench rates in this work. This implies slower cooling rates produce better Cu clusters with O being pushed away from them.

To compare the Cu-Cu and the Cu-O environment and its evolution during the *melt and quench* process in our models, we calculate, at each step, the following quantities:

$$d_{CuCu} = \frac{1}{3N_{Cu}} \sum_{i=1}^{N_{Cu}} \sum_{j=1}^{3} |\vec{R}_{Cu,i} - \vec{R}_{Cu,j}|, \quad (1)$$

$$d_{CuO} = \frac{1}{3N_{Cu}} \sum_{i=1}^{N_{Cu}} \sum_{j=1}^{3} |\vec{R}_{Cu,i} - \vec{R}_{O,j}|. \quad (2)$$

The sum over j runs over three nearest Cu in the first equation and over three nearest O in the second. The scatter plots in Fig. 3 show how these distances change as we cool the melt. This plot clearly shows that as we reduce the cooling rates, the O and Cu atoms move apart. Furthermore, the details of the change in the bonding environments of the atoms and the phase segregation of Cu atoms in the network during the *melt and quench* process has been discussed with animations in the supplemental material. There, we provide a visualization (carried out with OVITO software [31]) of the network formation process, and observe the exclusion of Cu in the host Ta_2O_5 network, rendering the Cu *atomus non grata* in or near the Ta_2O_5 regions. The main "takeaway" from Fig. 3 is that the more extended cooling produces a more compact Cu cluster for Model II [hence the extended right "leg" on the right side of the "ballerina plot" of Fig. 3(b) compared
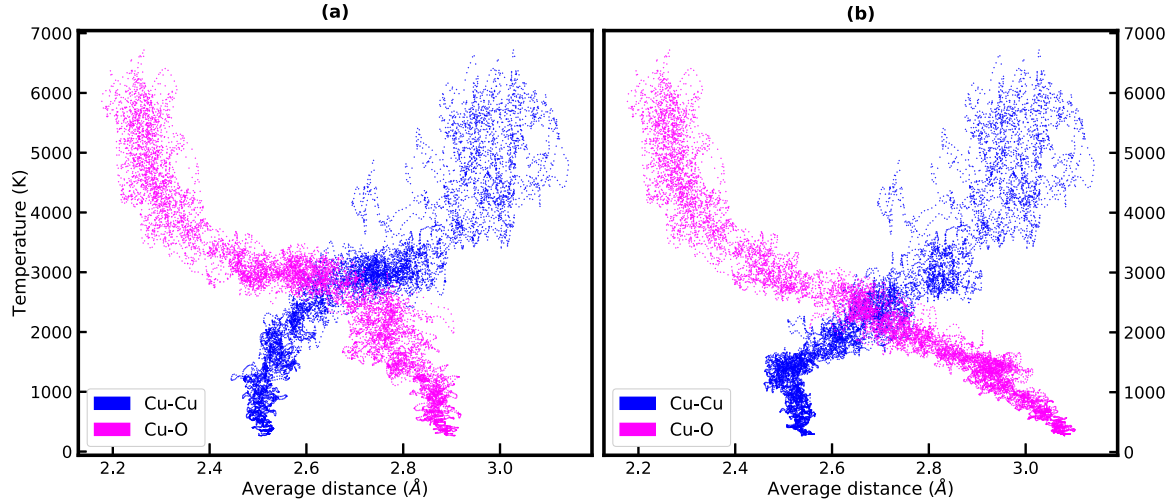
FIG. 3. Average distance of three nearest Cu to Cu atoms (blue dots) and O to Cu atoms (purple dots), averaged over all Cu atoms for Model I (a) and Model II (b).

to Fig 3(a)]. This suggests that slower cooling rates create Cu clusters that are as compact as possible and minimize Cu cluster surface area exposed to the Ta_2O_5 host. Of course, this hints at a propensity to form crudely spherical clusters, though our simulations are too small to prove this assertion.

B. Electronic properties

1. Electronic density of states

To understand the electronic structure of the models, we examine the total density of states (DoS), partial DoS, and inverse participation ratio (IPR). These calculations not only help us check the validity of the model but also can be used for *a priori* information to model amorphous materials [32,33]. The plot of the DoS in Fig. 4 reveals that both models have states around the Fermi level with extended Kohn-Sham orbitals indicating conducting behavior. Since the host (Ta_2O_5) is an insulator with a band gap of 4.22 eV [34], we see that the introduction of Cu to the network closes the gap by inducing impurity bands spread throughout the *entire* host (Ta_2O_5) gap. This is corroborated by the fact that the states near the Fermi level arise from the Cu $3d$ orbitals hybridized mainly with Ta and small contributions from O orbitals, as seen in the partial DoS plots in Fig. 4.

Our calculations show that the states near the Fermi level arise mostly due to Cu and Ta and a small contribution from O . The occurrence of Cu clusters in the Ta_2O_5 host suggest that the Cu clusters and Ta atoms near them form the conduction-active parts. In order to study the details of the states near the Fermi level, we plot the species-projected DoS averaged over three states above and below the Fermi level in Fig. 5. These plots show that states near the Fermi level arise from both Cu and Ta atoms and are shared among a fairly large number of atoms.

A further insight into the electronic properties is given by IPR defined as:

$$\mathcal{I}(\psi_n) = \frac{\sum_i |a_n^i|^4}{\left(\sum_i |a_n^i|^2\right)^2} \qquad (3)$$

with a_n^i being the contribution to the eigenvector ψ_n from the ith atomic orbital (s, p, and d) as obtained from VASP. In physical terms, IPR of electronic states is a measure of localization: localized state having high IPR value (ideally equal to $\mathcal{I} = 1$) while a completely extended state having a value of $(1/N)$, i.e., evenly distributed over N atoms. Near the Fermi level, we observe low IPR indicating delocalized states and conducting behavior of the models.

2. Space projected conductivity

The density of states provides some hints about the species contributing near the Fermi level; however, the conduction also depends on the localization of their electronic states and momentum matrix elements between Kohn-Sham states near the Fermi level. Recently, we have developed a spatial decomposition of the Kubo-Greenwood [35,36] formula that provides information about conducting paths in real space. By introducing a discrete grid in space, we show that the quantity:

$$\zeta(\mathbf{x}) = \left| \sum_{\mathbf{x}'} \Gamma(\mathbf{x}, \mathbf{x}') \right| \qquad (4)$$

provides such information at the spatial grid point $\mathbf{x}$ and for which:

$$\Gamma(\mathbf{x}, \mathbf{x}') = \sum_{ij\alpha} g_{ij} \xi_{ij}^\alpha(\mathbf{x}) [\xi_{ij}^\alpha(\mathbf{x}')]^*. \qquad (5)$$

Here g_{ij} is defined in Prasai *et al.* [16] and $\xi_{ij}^\alpha(\mathbf{x}) \equiv \psi_i^*(\mathbf{x}) p^\alpha \psi_j(\mathbf{x})$ is a complex-valued function, $\psi_i(\mathbf{x})$ is the ith Kohn-Sham eigenfunction, and $p^\alpha = \frac{\hbar}{i} \frac{\partial}{\partial x_\alpha}$, ($\alpha = x, y, z$). We have used this approach to describe transport in a solid electrolyte material [16] and Cu-doped amorphous alumina [37]. In a mixed (insulating/conducting) system like ours only a few eigenvectors of Γ characterize essentially all conduction in the system.

The SPC for both models is visualized as a grayscale plot in Fig. 6. The figure shows that connected Cu atoms form primary sites of conduction as expected. However, some
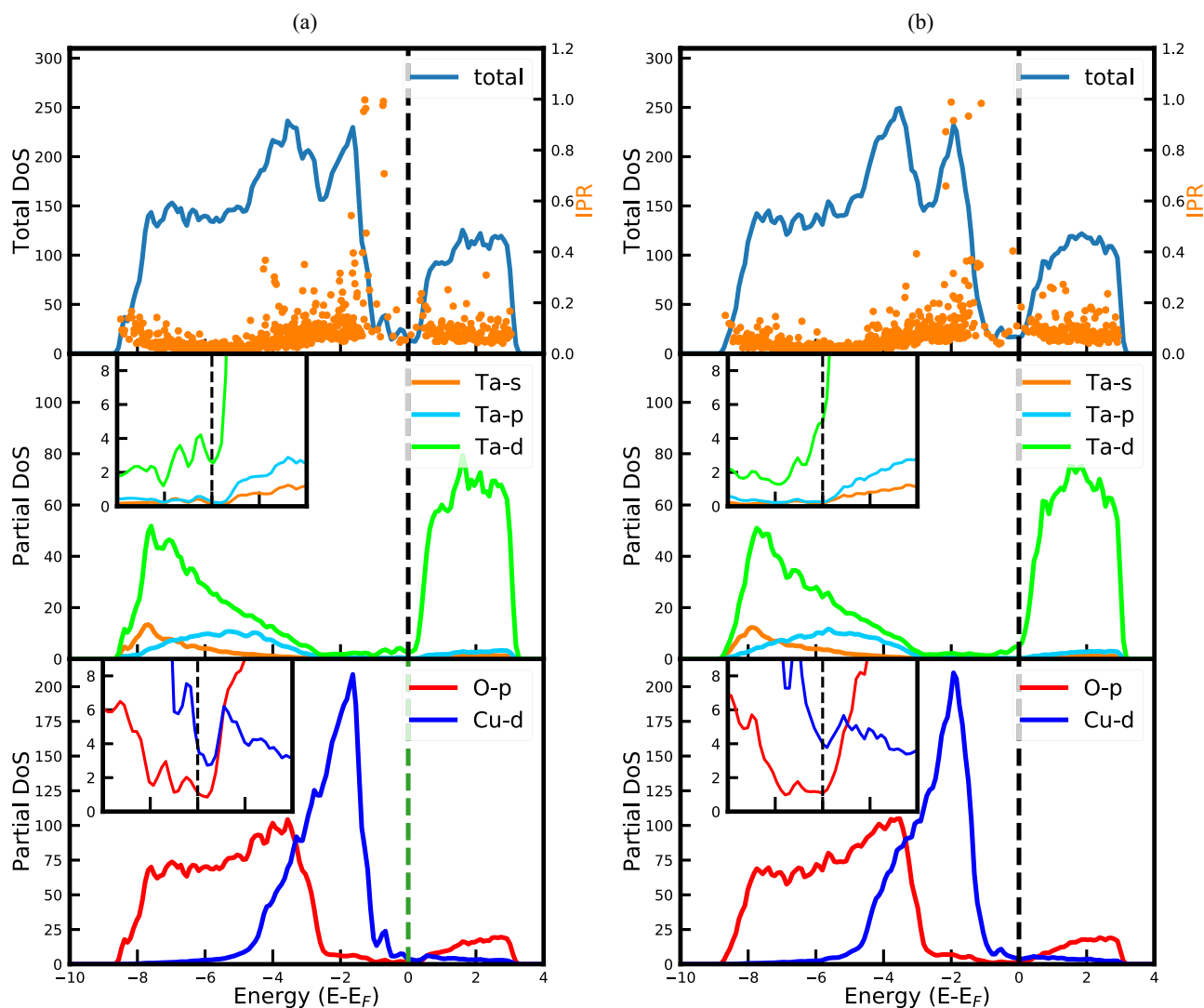
FIG. 4. Electronic density of (Kohn-Sham) states, inverse participation ratio and projection onto atomic species for Model I (a) and Model II (b) with black vertical drop lines indicating Fermi level. The insets show a magnified version of the DoS contributions from each species near the Fermi level.

Ta atoms, which are near the Cu atoms also contribute significantly to the electronic conduction. A detailed analysis of the bonding environment of these Ta atoms show that they are undercoordinated with oxygen, i.e., have less than (or equal to) five O bonds, a result that in agreement with

previous works on nonstoichiometric tantala [38]. A detailed discussion of the bonding environment and the coordination statistics of these Ta atoms has been made in the supplemental material. Furthermore, slower cooling rates produces higher Cu-Cu coordination and better connectivity, thereby
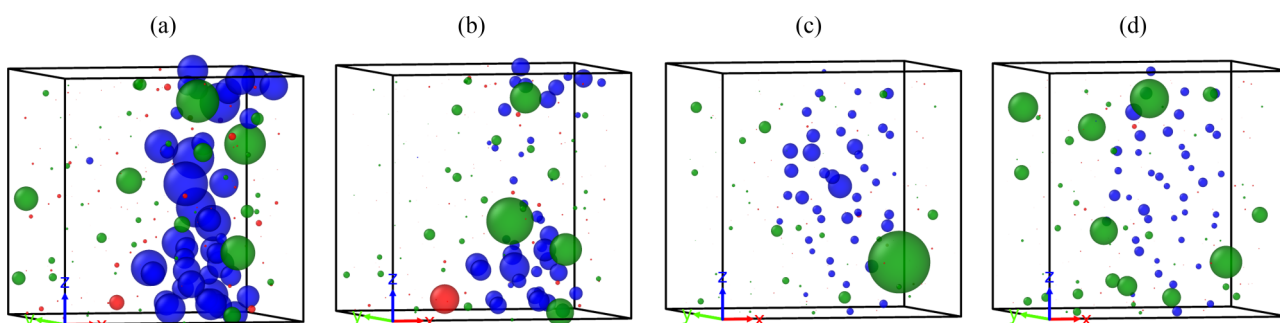

FIG. 5. Electronic DoS averaged over three bands below [(a) for Model I and (c) for Model II] and above [(b) for Model I and (d) for Model II] the Fermi level. The size of the atoms is proportional to their contribution to the total DoS. Colors as in Fig. 1.
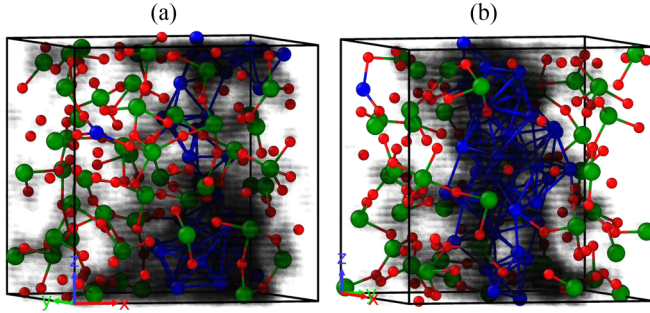
FIG. 6. Space projected conductivity scalar field for Model I (a) and Model II (b) shown in grayscale. Those parts of the network containing the interlinked Cu atoms are clearly more conducting in both models. The electrical conductivity of Model II is about 5 times that of Model I, because of the more robust Cu filament of Model II.

enhancing conductivity. There is a factor of about 5 higher conduction in Model II than Model I, presumably because of the small "neck" interlinking Cu in Model I.

C. Vibrational properties

1. Vibrational density of states

The vibrational density of states (VDoS) provides key information about local bonding environments in amorphous solids and serves as a test to validate a model [39]. Model I was well relaxed, and the lattice vectors were simultaneously relaxed to attain zero pressure, which of course produces a slightly nonorthogonal supercell. We displaced each atom in six directions ($\pm x$, $\pm y$, $\pm z$) by (0.015 Å), and after each of these small displacements, forces were computed on all atoms to obtain the force constant matrix and dynamical matrix [40]. Classical normal modes were computed from the dynamical matrix by direct diagonalization. The VDoS is defined as:

$$g(\omega) = \frac{1}{3N} \sum_{i=1}^{3N} \delta(\omega - \omega_i), \qquad (6)$$

with N and ω_i representing the number of atoms and the eigenfrequencies of normal modes, respectively. To determine the elemental contribution to the VDoS, we computed species
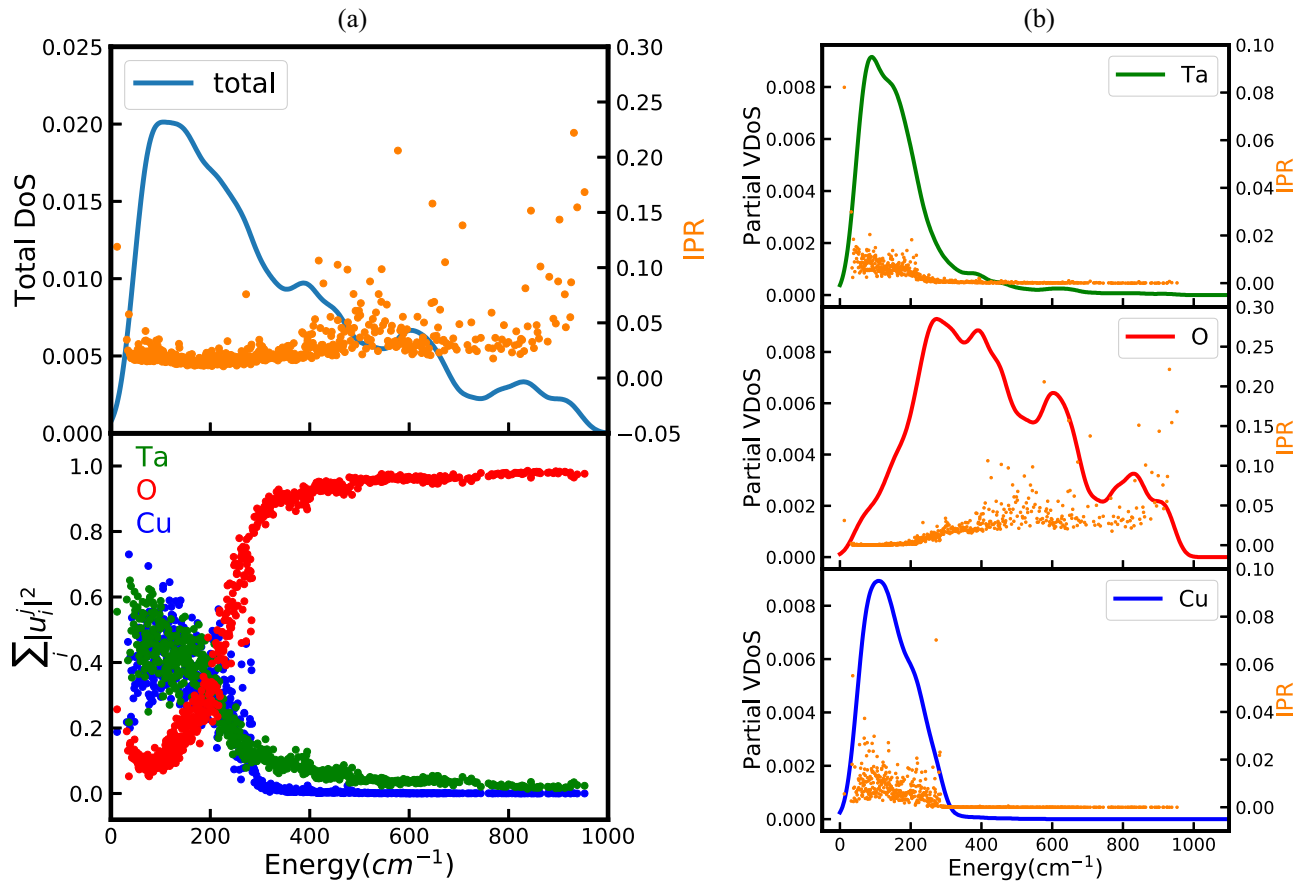

FIG. 7. (a, top) Total vibrational density of states for the Cu-doped Ta$_2$O$_5$ (Model I) and the magnitude of normalized eigenvectors averaged over atomic species ($|u_i^j|^2$) in (a, bottom). A transition is seen at frequency $\sim$270 cm^{-1}, where the oxygen atoms start dominating the vibrational spectrum. The total vibrational localization (IPR) in (a, top) shows that phonons modes are mostly extended with few localized modes appearing at higher frequencies. The yellow circles show IPR that indicates localization of vibrational eigenmodes. (b) We plot species-projected VDoS and VIPR of our Model I. We observe that oxygen dominates the higher-frequency range and the Cu subnetwork modes are mostly extended in nature.

projected VDoS defined as [41]:

$$g_\alpha(\omega) = \frac{1}{3N} \sum_{i=1}^{N_\alpha} \sum_n |e_i^n|^2 \delta(\omega - \omega_n), \qquad (7)$$

where $|e_i^n|^2$ are the eigenvectors of the normal modes and N_α is total number of atoms of α species. These species-projected VDoS must satisfy the relation $g(\omega) = \sum_\alpha g_\alpha(\omega)$. Like all supercell computations of normal modes, the low-frequency behavior is significantly affected by the small size of the cell and the small-k acoustic modes are not properly reproduced [42].

As seen in Fig. 7 (left), the VDoS is peaked at $\sim 105\,\mathrm{cm}^{-1} \approx 13\,\mathrm{meV}$, a peak arising due to the mixing of vibrational motion of Ta and Cu atoms. Partial VDoS plot (right panel) shows that Ta and Cu vibrations are both peaked at $\sim 105\,\mathrm{cm}^{-1}$ while the O atoms do not contribute to low-frequency vibrations as significantly as the other species. However, at frequencies above $\sim 400\,\mathrm{cm}^{-1}$, VDoS contributions arise mainly from the O atoms, with no mixing, which can be ascribed to the low atomic mass of O compared to Cu and Ta atoms. In the intermediate region ($200\,\mathrm{cm}^{-1}$-$320\,\mathrm{cm}^{-1}$), vibrations arise from combined contributions of all atomic species. Animations of selected modes are provided in the supplemental material. Mode mixing and cross-talk between the phase-separated regions are features of these animations.

2. Localization of vibrational modes

While the VDoS is an observable that can be measured almost directly from inelastic neutron scattering experiments, the localization of these vibrations is not easily observable. To study the localization of vibrational modes in the Cu-doped Ta$_2$O$_5$, we calculate the vibrational IPR, the vibrational analog of the electronic IPR, from the eigenvectors as shown in Eq. (8):

$$\mathcal{V}(\omega_n) = \frac{\sum_{i=1}^N |\mathbf{u}_n^i|^4}{\left(\sum_{i=1}^N |\mathbf{u}_n^i|^2 \right)^2}, \qquad (8)$$

where $(\mathbf{u}_n^i)$ is displacement vector of ith atom at normal mode frequency ω_n.

A small value of VIPR indicate evenly distributed vibration among the atoms while higher values imply only a few atoms contributing at that particular eigenfrequency. We have plotted the total VIPR in Fig. 7. Low values of VIPR below $\sim 300\,\mathrm{cm}^{-1}$ suggest that the vibrational modes are completely delocalized/extended. Above $300\,\mathrm{cm}^{-1}$, we observe higher VIPR. To provide visual insight to the spread of vibration over atoms and localization of some vibrational modes, suitable animations and explanations of some normal modes has been provided in the supplemental material.

To investigate the relation between the vibrational localization and atomic species, we evaluate contribution to VIPR from each atomic species, commonly called species-projected

VIPR. These projections sum to the total VIPR, i.e., satisfy the relation:

$$\mathcal{V}(\omega_n) = \mathcal{V}_{\mathrm{Ta}}(\omega_n) + \mathcal{V}_{\mathrm{O}}(\omega_n) + \mathcal{V}_{\mathrm{Cu}}(\omega_n) \qquad (9)$$

and is shown on the right panel of Fig. 7. The species-projected VIPR calculations suggest that low-frequency modes arise mainly from Ta and Cu atoms while the high-frequency vibrations come mostly from the O atoms which can be attributed to the atomic masses of the species. Higher values of partial VIPR are seen at higher frequencies. Therefore, the high-frequency modes are localized on a few O atoms in the network while the low-frequency modes are spread among larger number of Ta and Cu atoms. The quantity plotted in the bottom left panel in Fig. 7 is the squared magnitude of normalized eigenvectors summed across the atomic species for all the normal modes. The scatter plot and the partial VDoS plots suggest that the Ta and Cu atoms participate almost equally in the low-frequency vibrations.

IV. CONCLUSIONS

We describe the atomistic process of phase segregation of Cu in a-Ta$_2$O$_5$. Models made with a slower cooling rate revealed significantly better (denser) clustering than the one with faster cooling rate. These clusters, along with the neighboring undercoordinated Ta atoms, form a conducting path in the network which is in agreement with previous literature, though presented in novel way in this paper, and not relying only on the Kohn-Sham states near the Fermi level but also the momentum matrix elements, a legacy of the current-current correlation functions of Kubo. All this lends significant insight into an important CBRAM material.

It is interesting to speculate on what would happen in larger models and different cooling rates. We might expect to see Cu blobs in the network, possibly spatially separated but potentially interconnected by some other conducting fabric, perhaps Cu nanowires (of essential interest of course for CBRAM applications). While direct simulations like this one is computationally impossible for so large a system, it provides potentially useful *a priori* information for modeling employing simpler interatomic interactions. Electronic DoS calculations show that Cu doping closes the gap in the DoS of pure a-Ta$_2$O$_5$ with extended Kohn-Sham orbitals around the Fermi level. Vibrational modes at low frequencies are shared among many Ta and Cu atoms while those at high frequency are quite localized and come only from O atoms.

[1] I. Valov, R. Waser, J. R. Jameson, and M. N. Kozicki, Nanotechnology **22**, 254003 (2011).

[2] G. Dearnaley, A. M. Stoneham, and D. V. Morgan, Rep. Prog. Phys. **33**, 1129 (1970).

[3] D. Lee, S. Oukassi, G. Molas, C. Carabasse, R. Salot, and L. Perniola, IEEE J. Electr. Dev. Soc. **5**, 283 (2017).

[4] W. Chen, S. Tappertzhofen, H. J. Barnaby, and M. N. Kozicki, J. Electroceram. **39**, 109 (2017).

[5] T. Tsuruoka, K. Terabe, T. Hasegawa, and M. Aono, Nanotechnology **21**, 425205 (2010).

[6] T. Gu, T. Tada, and S. Watanabe, ACS Nano **4**, 6477 (2010).

[7] X. Xu, J. Liu, and M. P. Anantram, J. Appl. Phys. **116**, 163701 (2014).

[8] S. C. Pandey, R. Meade, and G. S. Sandhu, J. Appl. Phys. **117**, 054504 (2015).

[9] K. Chen, M. Nielsen, G. R. Yang, E. J. Rymaszewski, and T.-M. Lu, J. Electron. Mater. **26**, 397 (1997).

[10] S. Reid and I. W. Martin, Coatings **6**, 61 (2016).

[11] K. Prasai, J. Jiang, A. Mishkin, B. Shyam, S. Angelova, R. Birney, D. A. Drabold, M. Fazio, E. K. Gustafson, G. Harry, S. Hoback, J. Hough, C. Levesque, I. MacLaren, A. Markosyan, I. W. Martin, C. S. Menoni, P. G. Murray, S. Penn, S. Reid, R. Robie, S. Rowan, F. Schiettekatte, R. Shink, A. Turner, G. Vajente, H. P. Cheng, M. M. Fejer, A. Mehta, and R. Bassiri, Phys. Rev. Lett. **123**, 045501 (2019).

[12] T. Gu, Z. Wang, T. Tada, and S. Watanabe, J. Appl. Phys. **106**, 103713 (2009).

[13] B. Xiao, T. Gu, T. Tada, and S. Watanabe, J. Appl. Phys. **115**, 034503 (2014).

[14] N. Banno, T. Sakamoto, N. Iguchi, M. Matsumoto, H. Imai, T. Ichihashi, S. Fujieda, K. Tanaka, S. Watanabe, S. Yamaguchi, T. Hasegawa, and M. Aono, Appl. Phys. Lett. **97**, 113507 (2010).

[15] T. Tsuruoka, I. Valov, S. Tappertzhofen, J. van den Hurk, T. Hasegawa, R. Waser, and M. Aono, Adv. Funct. Mater. **25**, 6374 (2015).

[16] K. Prasai, K. N. Subedi, K. Ferris, P. Biswas, and D. A. Drabold, Phys. Stat. Solidi Rapid Res. Lett. **12**, 1800238 (2018).

[17] R. Bassiri, K. B. Borisenko, D. J. H. Cockayne, J. Hough, I. MacLaren, and S. Rowan, Appl. Phys. Lett. **98**, 031904 (2011).

[18] O. L. G. Alderman, C. J. Benmore, J. Neuefeind, E. Coillet, A. Mermet, V. Martinez, A. Tamalonis, and R. Weber, Phys. Rev. Materials **2**, 043602 (2018).

[19] G. Kresse and J. Furthmuller, Phys. Rev. B **54**, 11169 (1996).

[20] M. Hacene, A. Anciaux-Sedrakian, X. Rozanska, D. Klahr, T. Guignon, and P. Fleurat-Lessard, J. Comput. Chem. **33**, 2581 (2012).

[21] M. Hutchinson and M. Widom, Comput. Phys. Commun. **183**, 1422 (2012).

[22] G. Kresse and D. Joubert, Phys. Rev. B **59**, 1758 (1999).

[23] J. P. Perdew, K. Burke, and M. Ernzerhof, Phys. Rev. Lett. **77**, 3865 (1996).

[24] S. Nosé, J. Chem. Phys. **81**, 511 (1984).

[25] N. Shuichi, Prog. Theor. Phys. Suppl. **103**, 1 (1991).

[26] D. M. Bylander and L. Kleinman, Phys. Rev. B **46**, 13756 (1992).

[27] See Supplemental Material at http://link.aps.org/supplemental/10.1103/PhysRevMaterials.4.064603 for the description of a third structural model of the material quenched more rapidly than in the main text, animations of the atomistic process of phase separation, and animations of specific vibrational modes of special interest.

[28] D. A. Drabold, Eur. Phys. J. B **68**, 1 (2009).

[29] B. Shyam, K. Stone, R. Bassiri, M. Fejer, M. Toney, and A. Mehta, Sci. Rep. **6**, 32170 (2016).

[30] N. Kim and J. F. Stebbins, Chem. Mater. **23**, 3460 (2011).

[31] A. Stukowski, Modell. Simul. Mater. Sci. Eng. **18**, 015012 (2010).

[32] K. Prasai, P. Biswas, and D. A. Drabold, Phys. Status Solidi A **213**, 1653 (2016).

[33] J. H. Los and T. D. Kühne, Phys. Rev. B **87**, 214202 (2013).

[34] X. Wu, S. Soss, E. Rymaszewski, and T.-M. Lu, Mater. Chem. Phys. **38**, 297 (1994).

[35] R. Kubo, J. Phys. Soc. Jpn. **12**, 570 (1957).

[36] D. A. Greenwood, Proc. Phys. Soc. **71**, 585 (1958).

[37] K. N. Subedi, K. Prasai, M. N. Kozicki, and D. A. Drabold, Phys. Rev. Materials **3**, 065605 (2019).

[38] R. J. Bondi, M. P. Desjarlais, A. P. Thompson, G. L. Brennecka, and M. J. Marinella, J. Appl. Phys. **114**, 203701 (2013).

[39] G. P. Lopinski, V. I. Merkulov, and J. S. Lanin, Appl. Phys. Lett. **69**, 3348 (1996).

[40] B. Bhattarai and D. A. Drabold, Carbon **115**, 532 (2017).

[41] A. Pasquarello, J. Sarnthein, and R. Car, Phys. Rev. B **57**, 14133 (1998).

[42] D. A. Drabold, Molecular dynamics simulations of network glasses, in *Insulating and Semiconducting Glasses*, edited by P. Boolchand (World Scientific, Singapore, 2000), pp. 607–652.